Pulmonary Fissure Detection in CT Images Using a Derivative of Stick Filter

Changyan Xiao*, Berend C. Stoel, M. Els Bakker, Yuanyuan Peng, Jan Stolk, and Marius Staring

Abstract—Pulmonary fissures are important landmarks for recognition of lung anatomy. In CT images, automatic detection of fissures is complicated by factors like intensity variability, pathological deformation and imaging noise. To circumvent this problem, we propose a derivative of stick (DoS) filter for fissure enhancement and a post-processing pipeline for subsequent segmentation. Considering a typical thin curvilinear shape of fissure profiles inside 2D cross-sections, the DoS filter is presented by first defining nonlinear derivatives along a triple stick kernel in varying directions. Then, to accommodate pathological abnormality and orientational deviation, a max‑min cascading and multiple plane integration scheme is adopted to form a shape-tuned likelihood for 3D surface patches discrimination. During the post-processing stage, our main contribution is to isolate the fissure patches from adhering clutters by introducing a branch-point removal algorithm, and a multi-threshold merging framework is employed to compensate for local intensity inhomogeneity. The performance of our method was validated in experiments with two clinical CT data sets including 55 publicly available LOLA11 scans as well as separate left and right lung images from 23 GLUCOLD scans of COPD patients. Compared with manually delineating interlobar boundary references, our method obtained a high segmentation accuracy with median F_1-scores of 0.833, 0.885, and 0.856 for the LOLA11, left and right lung images respectively, whereas the corresponding indices for a conventional Wiemker filtering method were 0.687, 0.853, and 0.841. The good performance of our proposed method was also verified by visual inspection and demonstration on abnormal and pathological cases, where typical deformations were robustly detected together with normal fissures.

Index Terms—Fissure segmentation, image enhancement, pulmonary fissure, stick derivative.

I. INTRODUCTION

PULMONARY fissures are double layers of invaginations of visceral pleura that anatomically separate the lungs into lobes and segments [1]. Interlobar fissures are the physical boundaries between pulmonary lobes, dividing the human lung into five lobes (three in the right lung and two in the left lung). Accessory fissures often occur between bronchopulmonary segments but may also enter subsegmental or interbronchial planes [2]. Pulmonary fissures are important landmarks for delineation of pulmonary anatomy, and have significant value in localization of lesions and assessment of disease processes [3]. Particularly, there is an increasing requirement for quantification of fissure integrity or completeness, which is closely relevant to lung disease characterization and can be calculated as the percentage of the interlobar border defined by a fissure [4], [5]. However, automated or computer-aided segmentation of pulmonary fissures in CT images is not an easy task. The main challenges come from complicating factors such as their thin, weak and variable structures, pathological deformation, inhomogeneous intensity, imaging noise along with interferences from adjacent vessels, bronchi and pathological structures (e.g., fibrotic tissue).

Several automatic or semi-automatic methods have been reported in the literature to realize pulmonary fissures segmentation. With the lung parenchyma segmentation, pulmonary airway and vessel trees extraction techniques gradually becoming mature [6], an indirect strategy is to utilize these detected tissues to guess the fissure position on the basis of some prior assumptions. Among them, the sparse distribution of vessels and bronchi in the neighborhood of fissures is commonly used anatomical knowledge, which has been integrated under different segmentation frameworks like the watershed transform [7], [8], Voronoi division [9], adaptive sweeping [10], minimal path [11] and neural network classifier [12]. Another more global constraint is integrated in lung atlas schemes including the single atlas search initialization [13] and a multi-atlas selection mechanism recently proposed by van Rikxoort *et al.* [14]. Although these indirect methods could provide an approximate estimation of the fissure position and thus help to reduce computational burden, the most reliable information still comes from the object itself. This is also the reason why the fissure appearance and shape characteristics are attracting more attention for accurate localization and refinement [15], [16].

Much effort has been made to efficiently exploit the direct fissure information. Based on the fact that the profile of pulmonary fissures across transverse planes can be approximated with piecewise straight lines, Kubo *et al.* [17] presented a 2D VanderBrug operator to enhance the linear structures and simultaneously suppress streak artifacts. Their method was later extended to 3D space as a sheet-emphasis filter [18]. Zhang *et al.* [13] began with a 2D ridgeness measure to enhance fissure contrast, the direction and intensity continuity was integrated

under a fuzzy reasoning framework to sift out the fissure objects. Wiemker *et al.* [19] proposed two equivalent fissure likelihood filters using structure tensors and Hessian matrices for shape description. A similar likelihood function was recently defined by Lassen *et al.* [15] and the plane filter of Li *et al.* [20] can also be considered a pilot method to enhance the fissure-like tissues. To automatically distinguish what should be enhanced or suppressed, van Rikxoort *et al.* [21] presented a supervised filter, which adopts a pattern recognition technique to select the most important features and was further harnessed to group the unordered structures into bigger fissure plates [22]. A computational geometry approach has been developed by Pu *et al.* [23], where they utilized a statistical approach to extract the pulmonary fissures in 3D space after iteratively smoothing the triangle meshes with a Laplacian filter. The same authors later suggested an anisotropic morphological operator as a post-processing method to smoothen fissure surfaces and fill small holes [24]. Furthermore, their method was improved by a piecewise plane fitting algorithm [16] to directly identify fissure patches from the original lung sub-volumes. Ross *et al.* [25] employed a particle system that samples the image domain and provides a set of candidate fissure locations based on image derivative features. A maximum a posteriori estimation was then applied to eliminate poor candidates and remove residual noise particles. Later, their ridge surface sampling scheme was merged with a lobe boundary shape model to improve fissure discrimination [26]. Recently, Kinder *et al.* [27] proposed a line enhancing filter as an extension to the previous Hessian filter [19]. Their method is close to our proposed filter but they used a single stick template.

Motivated by a line detection model in speckle images [28], we present a derivative of stick (DoS) filter for fissure enhancement with emphasis on direction estimation and interference suppression. The basic idea is to probe the presence of 2D fissure profiles across section planes by formulating it as a M-ary hypothesis testing problem, where a rectangle neighborhood is divided into various straight line-segments (i.e., sticks) corresponding to potential fissure directions. Different from traditional isotropic or spot kernel filters, our method defines a likelihood measure by investigating appearance feature along orienting templates, which make it more appropriate for extremely anisotropic and thin elongated structures. For subsequent segmentation, we introduce a post-processing pipeline based on connected component analysis, where multi-threshold binarized images are directly merged after removing adhering clutters with a branch-point detection algorithm.

In this paper, our main purpose was to extract pure fissure patches rather than generate a full lobe segmentation. This means that only the visible fissures on CT are extracted and no interpolation operation was applied to extend the fissure plane or fill its inner holes. An early version of this method has been presented at a conference [29]. In this current work, the algorithms are improved further and the experiments have been extended into a full validation. The remainder of the paper is organized as follows. In Section II, the methods are described in details. The data and reference are described in Section III. We give the experiment and evaluation results in Section IV, and in Section V the conclusions are presented.

II. METHODS

In this section, we present our framework for fissure detection, which consists of a fissure enhancement filter as well as a post-processing segmentation pipeline.

A. A Derivative of Stick Filter for Fissure Enhancement

As a distinct 3D planar or surface structure in human lungs, the pulmonary fissures possess some distinguishable shape and appearance features. If we cut a volume CT image with mutually orthogonal planes, the fissure profiles will typically appear as bright thin curvilines in at least two planes, see the normal fissure profiles in Fig. 1. This observation is considered an important property in our paper to discriminate the fissure patches from other pulmonary tissues. For example, small pulmonary vessels might happen to be a bright line inside a single transverse plane, but they hardly show similar shapes in other perpendicular sections. An exception is those vessel segments running parallel to a certain coordinate axis, which might simultaneously take a linear shape across two orthogonal sections. This will happen with low probability and is ignored in this paper.

Based on this observation, a fissure enhancement filter is developed. Although essentially a 2D filter, the 3D surface characteristics of fissures will be indirectly taken into account by merging information from orthogonal planes.

1) A Rotating Stick Kernel Transformation: A problem with pulmonary fissure detection in CT images is that they often appear to be a single pixel wide and even broken for several pixels. The traditional smoothing filters without a matched line shape constraint are inappropriate, because the thin and weak fissures are at risk of being swept out together with the noise [27].

Motivated by a line detection model in speckle images [28], we introduce a realistic method to probe the presence of 2D fissure profiles across each section plane by approximating them with piecewise straight line-segments called sticks. To adapt the direction change, a rotating kernel transformation [30] is introduced by first decomposing a rectangular neighborhood into single-pixel width and fixed length sticks, where each of them represents a potential fissure orientation. Typically, an $L \times L$ neighborhood can be decomposed into $2(L-1)$ sticks, which is done by spatially sampling and discretizing the rotating lines through the center, see Fig. 2 for an example of $L = 11$. Note this is essentially a $M-$ ary hypothesis testing problem with each hypotheses being a possible fissure or stick direction.

To some extent, the original single stick model can be considered as an extreme case of the anisotropic Gaussian filter, where the long axis scale is much larger than the short axis scale. To account for intensity variance or local discontinuities along the fissure, a rectangular window average rather than a Gaussian weighting is adopted to minimize the influence of the relative position.

Definition of Nonlinear Derivatives: Based on this rotating kernel transformation, our DoS filter is developed by further introducing a triple stick template instead of a single stick as the filtering kernel. Due to anatomically sparseness or lack of vessels and bronchi around lobar boundaries, the neighboring background on both lateral sides of the fissure often shows up as low-intensity strips on CT images. Taking this into account, we
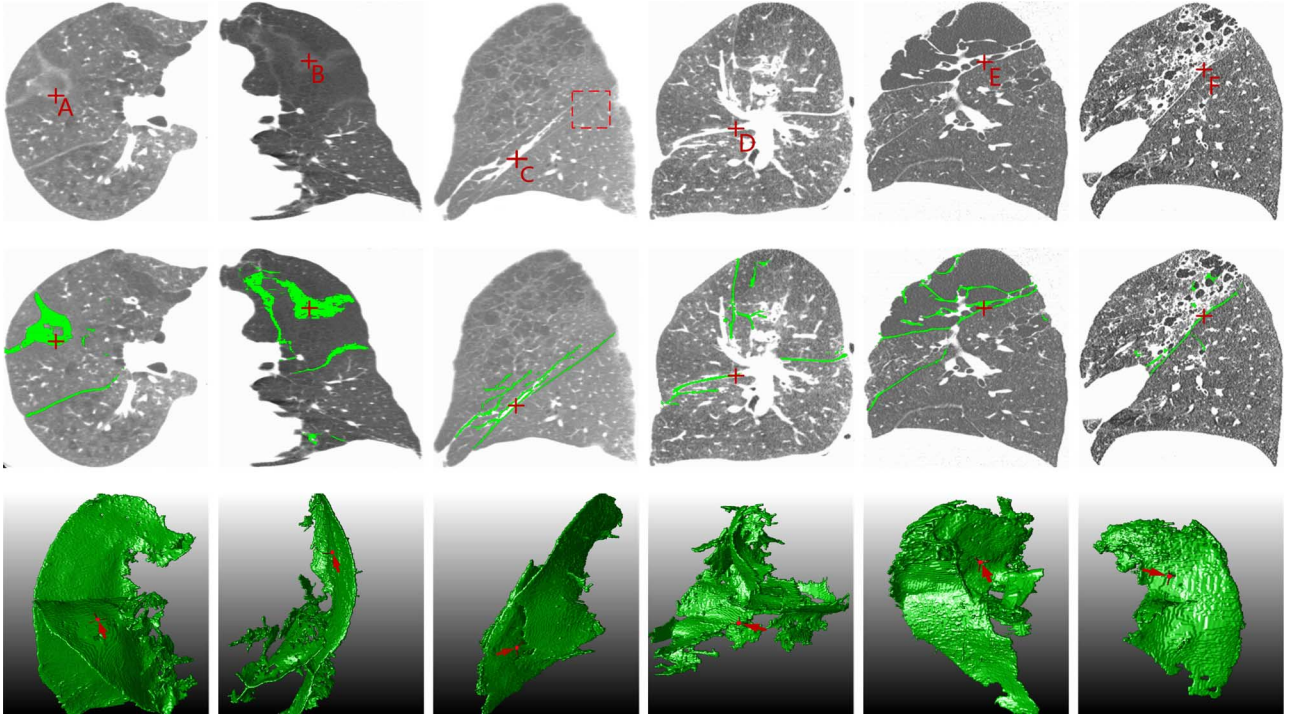
Fig. 1. Demonstration of pulmonary fissures segmentation using the proposed method in six different subjects. From top to bottom row, the original image slice, blending segmentation and 3D fissure surfaces are sequentially given. The segmented fissures are rendered in green. Several typical local abnormalities including orientational deviations (A and B), thickened fissures (C and D) and step deformations (E and F) are marked with red crosses, which are further highlighted using red arrows on the 3D surfaces. The red dashed rectangle region of Fig. 1(c) will be used later in Fig. 3 for stick derivatives description.
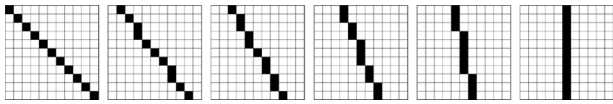

Fig. 2. Decompose a $L \times L$ rectangle neighborhood into $2(L-1)$ sticks. Here, $L = 11$ and the remaining sticks can be obtained by mirroring or rotating the listed ones.

propose to simultaneously probe the fissure profile and its close neighborhood using three parallel and slightly gapped sticks, see the triple-stick kernel overlaying fissure image region in Fig. 3. Here, the central sticks correspond to the single-stick kernels in Fig. 2. This is also the principle which human observers utilize to infer the presence of fissures especially for weak and noisy objects.

To give a mathematical expression, we use μ_M, μ_L and μ_R to indicate the mean intensity respectively along the middle (red), left (green) and right (blue) sticks of the kernel, see Fig. 3. The mean values of intensity are calculated with $\mu = 1/L \sum_{j=1}^{L} I_j$, where I_j is the intensity of the jth pixel along each stick. Then, two nonlinear derivatives perpendicular to the sticks can be defined as

$$\lambda_{\perp,\max}^{S,\theta}(\boldsymbol{x}) = \max(\mu_M - \mu_L, \mu_M - \mu_R) \qquad (1)$$

and

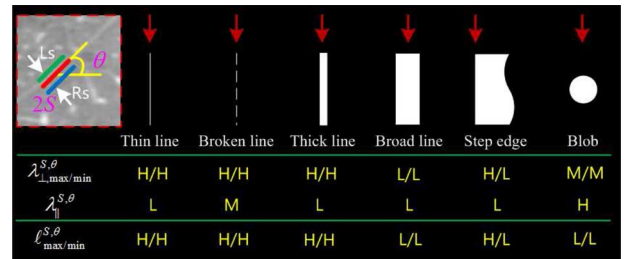$$\lambda_{\perp,\min}^{S,\theta}(\boldsymbol{x}) = \min(\mu_M - \mu_L, \mu_M - \mu_R), \qquad (2)$$

Fig. 3. Analyzing the performance of the stick derivatives on various pulmonary tissues. Here, we use the thin, thick and broad lines to depict the curvilinear structures with width increasing from single-pixel to larger than $2S$. At the top-left, a triple-stick kernel with L_s being the left stick and R_s the right one is overlaid on a small fissure region from Fig. 1, and the top red arrows denote its detection locations along various structures. The responses of derivative operators and line strength measures are listed on the second and third rows, where H, M and L represent a high, medium and low value, respectively.

where S denotes the spacing between adjacent sticks, θ is the orientation angle and $\boldsymbol{x}$ the spatial location in the lung. With a spacing S involved in the template, the derivative operators are less sensitive to partial volume effect and allow the fissures with varying width or blurred boundaries to be equally well detected. The main difference between $\lambda_{\perp,\max}^{S,\theta}$ and $\lambda_{\perp,\min}^{S,\theta}$ lies in their performance on step edges. The former is particularly designed to enhance the step-shaped abnormal fissures (see Figs. 1E and 1F), while the latter tends to suppress them.

Although the above derivative operators are originally defined on a triple stick kernel, their computation can be simplified by introducing a spatial shifting scheme, i.e., the μ_L and μ_R can be approximated with the middle stick average μ_M at displaced

positions. More clearly, using (x_1, x_2) to denote the 2D coordinates in the cross-section, we have

$$\mu_L^\theta(x_1, x_2) = \begin{cases} \mu_M^\theta(x_1, x_2 - S), & -\frac{\pi}{4} < \theta \leqslant \frac{\pi}{4} \\ \mu_M^\theta(x_1 - S, x_2), & \frac{\pi}{4} < \theta \leq \frac{3\pi}{4} \end{cases} \quad (3)$$

and

$$\mu_R^\theta(x_1, x_2) = \begin{cases} \mu_M^\theta(x_1, x_2 + S), & -\frac{\pi}{4} < \theta \leqslant \frac{\pi}{4} \\ \mu_M^\theta(x_1 + S, x_2), & \frac{\pi}{4} < \theta \leq \frac{3\pi}{4} \end{cases}. \quad (4)$$

Here, the shifting coordinate is chosen depending on the orientation θ of the middle stick, and a range of $\theta \in (-\pi/4, 3\pi/4]$ is used for conciseness. In other words, we only need to shift the first coordinate for roughly vertical sticks and the second one for approximately horizontal sticks.

To illustrate the performance of $\lambda_{\perp,\max}^{S,\theta}$ and $\lambda_{\perp,\min}^{S,\theta}$, several idealized shapes representing different pulmonary tissues are given in Fig. 3. For both operators, the thin, broken and thick lines corresponding to normal fissures with different widths will get a high response; the broad line, which indicates an axial profile of large vessels, will be neglected with a low response. However, a difference will occur on the step-edge used to depict an over-thickened fissure: the $\lambda_{\perp,\max}^{S,\theta}$ will get a full response, but the $\lambda_{\perp,\min}^{S,\theta}$ has a null response. As for the blob-shaped interferences such as the transversal profile of vessels, both derivatives will neither give a full response nor a zero response, i.e., obtain a medium value.

To further suppress the undesired blob shape, we introduce a second measure $\lambda_{\parallel}^S$ equal to the intensity standard deviation along the middle stick, i.e.,

$$\lambda_{\parallel}^{S,\theta}(\boldsymbol{x}) = \sqrt{E[I_j^2] - (E[I_j])^2}. \quad (5)$$

Here, E indicates an expected value operator and I_j the intensity of the jth pixel along the middle stick. The utilization of intensity variance to detect line edges was inspired by our previous work [31]. Like the effect of Hessian values in shape description [32], [33], $\lambda_{\perp}^s$ and $\lambda_{\parallel}^s$ also reflect the local contrast along the elliptical axes while used for geometric representation. Accordingly, two 2D line strength measures, $\ell_{\max}$ and $\ell_{\min}$, can be formulated as

$$\ell_{\max/\min}^{S,\theta}(\boldsymbol{x}) = \lambda_{\perp,\max/\min}^{S,\theta}(\boldsymbol{x}) - \kappa \cdot \lambda_{\parallel}^{S,\theta}(\boldsymbol{x}). \quad (6)$$

Here, κ is a positive coefficient to adjust the sensitivity to axial intensity inhomogeneity. Obviously, the blob structure will get a low response for both $\ell_{\max}$ and $\ell_{\min}$ due to its large intensity variation along the stick. On the contrary, all the line structures will obtain a high response if using a suitable κ parameter (e.g., $\kappa \in (0, 1]$), see Fig. 3 for details.

2) Multi-Direction Integration: As depicted in Fig. 2, an $L \times L$ rectangular neighborhood can be decomposed into $2(L-1)$ sticks. Correspondingly, there exist $2(L-1)$ possible orientations for the triple stick templates. We choose the template with the maximum response of $\ell_{\max}$ or $\ell_{\min}$ as the optimal kernel. Thus, the multiple directional information can be integrated with

$$F_{\max/\min}(\boldsymbol{x}) = \max\left(\max_{1 \leq i \leq 2(L-1)}\left(\ell_{\max/\min}^{S,\theta_i}\right), 0\right). \quad (7)$$

Here, θ_i indicates the discrete angle of the ith stick around its rectangular neighborhood. Because we are only interested in bright objects, only non-negative response values are considered. Like the vesselness function in [33], $F_{\max}$ and $F_{\min}$ are equal to a 2D fissure likelihood with their optimal kernel orienting along the fissure profile.

A similar method called the tram-line filter has been presented early by Hunter *et al.* [34] for retinal vessel segmentation. Our DoS method differs from their filter in that we inherit a shape description idea from previous curviline filters [35], which makes it possible to distinguish between various pulmonary structures.

3) Max-min Cascaded Filtering: From the literature, most existing fissure filters only handle normal line or plane shaped fissures. However, as shown in Fig. 1, a typical abnormality is that the fissure profiles might take a step shape due to asymmetric intensity across lobes or appear as a thickened band arising from adjacent condensed vascular tissues (e.g., Fig. 1C). In our previous implementation [29], only the $\lambda_{\perp,\min}^{S,\theta}$ derivative was utilized in fissure likelihood calculation, which unfortunately takes a low response on these abnormalities and will finally result in a missed detection.

To handle this problem, we combined the $F_{\max}$ and $F_{\min}$ of (7) in a cascaded way. The basic principle is that the step-like or thickened fissure can be first transferred into a standard thin curvilinear structure by applying the $F_{\max}$ transformation. Then, with a subsequent $F_{\min}$ operation on the result of the $F_{\max}$ filter, both normal and abnormal fissures can be equally well enhanced. Accordingly, the combined filter is written as

$$F_\circ = F_{\max} \circ F_{\min} \quad (8)$$

with $\circ$ being the cascading operator, which means the $F_{\min}$ is applied after the $F_{\max}$ filtering. Due to the effect of $F_{\max}$, the step-shaped deformation as marked in Fig. 1F can now be treated like a normal fissure. But the thickened fissure with a width larger than $2S$ is handled more like two parallel step-edges, where the $F_\circ$ responds simultaneously to both its lateral sides, see Fig. 1C for example. For normal fissure profiles, the $F_\circ$ operator actually works like a twice iteration of our previous $F_{\min}$ filter [29], as $F_{\max}$ and $F_{\min}$ take similar performance in the cases. Since the $F_{\min}$ has an inherent property on suppressing broad objects, it is guaranteed that the filtered structures will take approximately homogeneous thickness (less than $2S$) and thus benefit the morphology analysis in post-processing segmentation. Here, we do not force a direction consistency between $F_{\max}$ and $F_{\min}$ kernels, because some local orientation deviations could be self-corrected through the cascading iteration.

4) Multiple Cross-Sections Integration: In clinical CT scans, many complex factors exist, such as anisotropic resolution, inhomogeneous intensity, largely varying shape and orientation, which make it difficult to completely detect the 3D fissure surface only from a single plane. For instance, in Figs. 1A and 1B, the fissure patches marked with red crosses take a vague band appearance due to their orientation running approximately along the cross-sections. Since the profiles deviate largely from a stan-
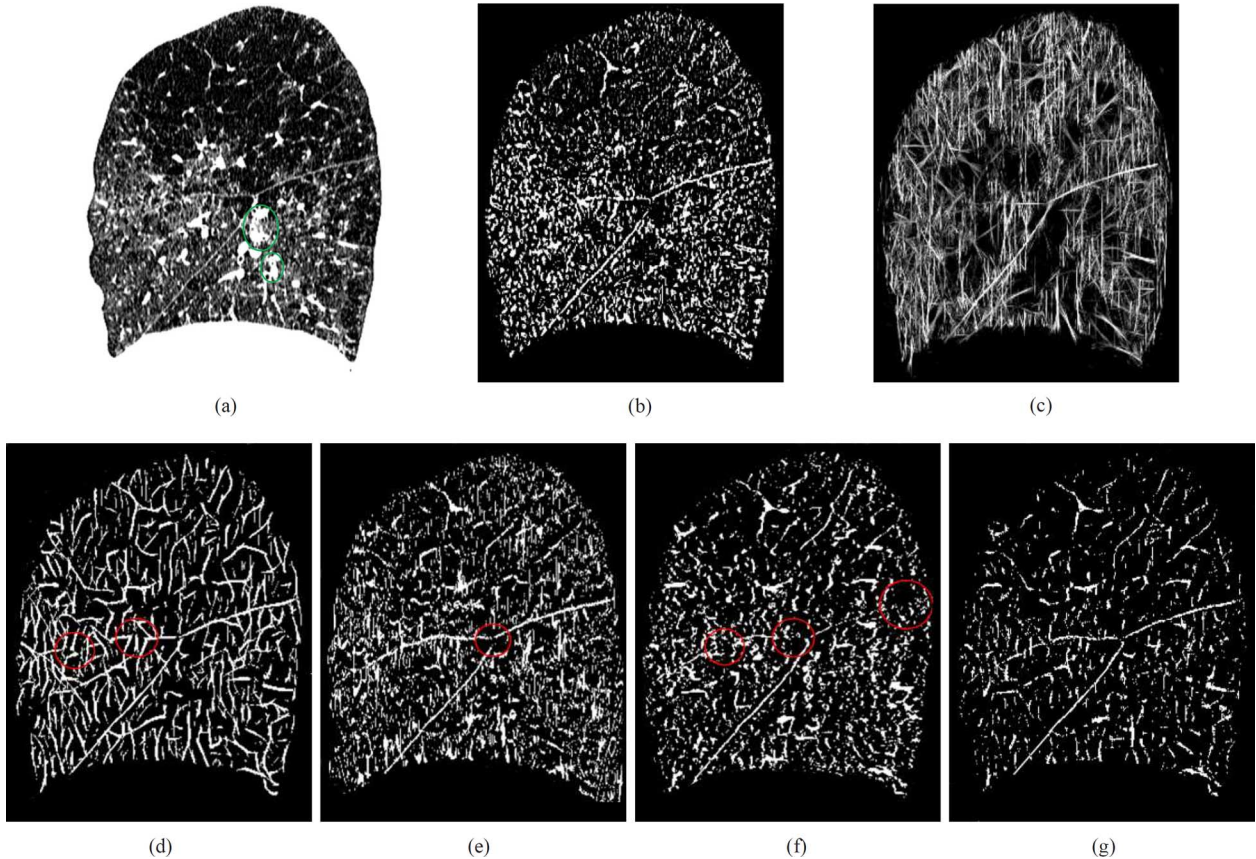
Fig. 4. Applying the cascaded filter $F_\circ$ with parameters $L = 11$, $S = 3$, and $\kappa = 0.7$ to the LOLA11–12 scan along the Sagittal, Coronal and Axial cross-sections, respectively. Here, (a) indicates a sagittal slice (No. 347) of the original volume image, (b) and (c) are its results respectively from the Wiemker [19] and Klinder filters [27]. The $F_\circ$ responses from the three different orientations and their shape-tuned accumulation F^{3D} are sequentially given in (d)-(g). The red circles mark the missed fissure regions in the 2D filtered images. (a) Original image (b) Wiemker filter (c) Klinder filter (d) $F_\circ^S$ (e) $F_\circ^C$ (f) $F_\circ^A$ (g) F^{3D}.

dard curvilinear shape, they are suppressed by the $F_\circ$ filter if applied to the current plane.

Considering these complex factors, we propose to merge the $F_\circ$ responses from multiple cross-sections in different directions. The idea is to compensate local discontinuity or deformation by consulting line detection from other cutting planes based on an implicit 3D co-planar assumption. For example, a fissure patch might happen to be broken along the axial cross-section, but its well-developed profiles in the sagittal and coronal planes still make it a detectable object.

Although there are many choices to achieve multi-section integration, we adopt a 3D shape-tuned fissureness function, i.e.,

$$F^{3D}(\boldsymbol{x}) = (F_\circ^A + F_\circ^S + F_\circ^C) \cdot \frac{F_\circ^2}{F_\circ^3}. \qquad (9)$$

Here, $F_\circ^A$, $F_\circ^S$ and $F_\circ^C$ indicate the $F_\circ$ responses from the axial, sagittal and coronal cross-sections, respectively, and all have nonnegative values. Sorting the three responses in $F_\circ^1 \le F_\circ^2 \le F_\circ^3$, their ratio $F_\circ^2/F_\circ^3$ can work as a shape description term. Generally, the 3D fissure patches will respond strongly to at least two $F_\circ$ measures across the three orthogonal planes. In contrast, the interference structures like pulmonary vessels usually produce at most one single large $F_\circ$ value due to their unidirectional property. Based on this, the ratio $F_\circ^2/F_\circ^3$ will take a high value close to 1 on the planar fissures and typically tends to zero for

undesired tube clutters. Correspondingly, the accumulation of the three $F_\circ$s can be considered a structure strength. Therefore, Eq. (9) is essentially a shape-tuned structure likelihood for 3D fissures discrimination.

As an example, a sagittal slice from a pulmonary CT scan and its filtered results are illustrated in Fig. 4. For the 2D $F_\circ$ responses, different kinds of openings (false negatives) marked with red circles can be seen in Figs. 4(d)–4(f), which means none of the single cross-section filters can obtain a complete result. But the F^{3D} image in Fig. 4(g) combines them into a more complete fissure detection. Not only the fissure profiles have been well enhanced, but also the vascular clutters and blob interferences (see the green circles in Fig. 4(a)) are saliently suppressed. For comparison, the responses from a Wiemker Hessian filter [19] and a Klinder filter [27] are given in Figs. 4(b) and 4(c), which will be elaborated later in Section IV. Here, both filters cannot discriminate between fissures and vessel profiles, and obvious over-detections are seen in Fig. 4(c). Although the Klinder filter appears to detect a majority of the fissure profiles, the dense adhering clutters simultaneously increase the difficulty of subsequent segmentation.

In contrast to other template matching methods [16], [18], no explicit 3D model is involved in our F^{3D} filter. But the curvilinear shape constraint across multiple sections can be considered a realistic simplification of a 3D co-planar assumption and its obvious merit is a decrease of computational burden. In this
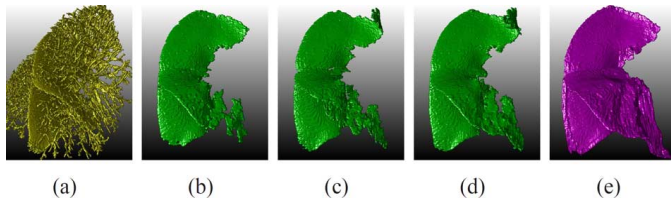
Fig. 5. Demonstration of post-processing segmentation. Here, a direct binarization of the F^{3D} image is given in (a). Figures (b) and (c) depict the two single-threshold segmentations of fissures using different thresholds $Th = 1$ and 20. The proposed multi-threshold merging result with $Th = 1, 5, 10, 20, 40$ and 60 is visualized in (d), and (e) is the interlobar boundary reference.

way, the inherent 3D surface constraint of fissures has been divided into two parts with the 3D connectivity analysis being migrated towards the subsequent post-processing stage.

B. A Post-Processing Pipeline for Segmentation

Although the proposed DoS filter can efficiently enhance pulmonary fissures in CT images, a remaining problem is that still some undesired structures are simultaneously enhanced, making a simple threshold segmentation unfeasible. This is especially important when those residual clutters are connected to fissures. To demonstrate this, a binarization of the F^{3D} filter response using a global threshold is given in Fig. 5(a): the intensive interferes partially occlude the fissures and make them indiscernible.

As a solution, a relatively simple post-processing pipeline is presented. Ascribing to the lateral suppression effect of F_{min} operators, the pulmonary structures have generally been thinned to a width less than $2S$ in the filtered image, and the residual clutters are only sparsely linked to the fissure surface at a few locations, see Fig. 5(a). From this observation, we propose to isolate the fissure patches from adhering clutters by directly breaking their connective branch-point or junction regions. Moreover, considering the inhomogeneity of intensity, a multi-threshold merging framework is introduced to overlap the isolated fissures from different binarizations for more complete segmentation. Before the post-processing segmentation, we utilize a lung mask to eliminate unrelated interferences from neighboring tissues like ribs.

The whole post-processing pipeline consists of five steps (schematically shown in Fig. 6), and the detailed algorithms are given as follows:

1) In Step 1, a group of global thresholds $b_i(i = 1, \ldots, n)$ is used to binarize the F^{3D} image. As shown in Fig. 6 there is no single threshold that yields the complete fissure without over-segmentation. A relatively low threshold (b_1) will extract the complete fissure, but simultaneously lead to more noise. On the contrary, a high threshold (b_n) might miss some weak parts of the fissure (see the gap in b_n), but less clutter is selected. We therefore adopt a multi-threshold framework to accommodate for local intensity variation.

2) We proceed to remove all the branch points from each of the binarized results. To ensure a complete deletion of 3D junctions, without breaking the global connectivity of fissure patches, we apply branch removal in 2D sections on each of the three orthogonal directions successively. As the fissure patches are essentially 3D plate-like structures, the

removal of local 2D junction regions will seldom affect their connectivity in 3D. Pulmonary vessels and bronchi, however, frequently dominate in a single direction, and are therefore split into small fragments. In detail, we first employ a 2D morphological skeletonization to extract the centerlines of elongated structures on each binarized 2D section. Subsequently, using a set of 8-neighborhood look-up tables to represent the possible branching patterns, all the branch points along the centerlines can be found with a simple match algorithm [36]. A circular region around each branch point with radius S is then removed from the binarized results from step 1.

3) After removal of the branch point regions, the fissure patches become mostly separated from other structures. To prevent these structures from relinking to the fissures in a later step, we remove small components (see the green short-lines in the dashed rectangle) from each of the 3D junction-removed images, using a volume threshold vT (e.g., 100 voxels for a left or right lung) throughout this paper. Subsequently, these purified images are merged into a single binary image using an OR logical operation. Because junctions and small noisy structures were eliminated beforehand, the isolation of fissure patches is kept after the merging step.

4) A 3D connected component analysis is used to automatically select the fissure patches as the largest N (e.g., 20) objects, thereby sifting out smaller structures. In Fig. 6, the selected fissure patches are drawn in black and clutters in red lines. Instead of component volume more elaborate selection measures may be devised for this step, but we will show that the volume selection criterion yields satisfactory results.

5) To complete the post-processing we put the previously removed branch points back, to fill the small holes resulting from step 2. We only restore those branch points that belong to the finally selected patches. This is achieved by dilating the current result using a spherical structure element with radius S, and subsequently using this dilated image as a mask to select branch points (blue solid circles) within the mask.

To illustrate the merit of the multi-threshold merging framework, two single-threshold segmentations also using the branch-point removal and hole-filling strategy are shown in Figs. 5(b) and 5(c), and the proposed multi-threshold result is given in Fig. 5(d). Compared to the manual interlobar boundary reference in Fig. 5(e), both single-threshold methods resulted into incomplete detection but the missing parts appear to vary in locations. With the complementarity among different binarizations, the multi-threshold scheme resulted into more complete segmentations. Recently, a similar multi-threshold edge grouping framework was proposed by Papari and Petkov [37] for 2D contour detection. Although partially inspired by their idea, our method differs in some critical steps like branch-point removal, and 3D shape guided clutter pruning. Our main contribution on the post-processing is to achieve clutter removal by employing the difference of shape and geometry between fissure and tube structures. This idea is applied to pulmonary fissure segmentation probably for the first time.
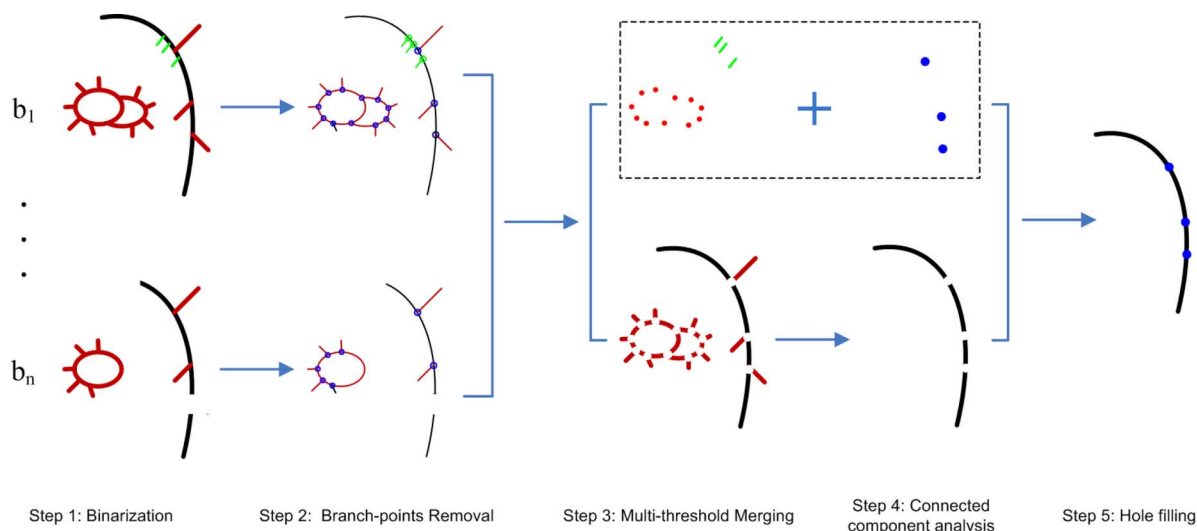
Fig. 6. Overall flowchart of the post-processing pipeline. Here, the black curves indicate the real fissures with the red ones being clutters, and the green short lines denote noisy spurs. The green open circles represent the branch-points caused by adhering spurs and the blue open circles being typical junctions from clutters. The dashed rectangle marks the removed junctions (solid circles) and small clutters (green short-lines).

Since our method was particularly designed to accommodate some fissure abnormalities, it is necessary to check its performance in experiments. As mentioned before, several typical deformations are illustrated in Fig. 1. Here, marks A and B indicate two irregular fissure bands caused by orientation deviation falling inside the section planes. Mark C and D denote two thickened fissures usually arisen from dense vessel tissues. We use E and F to depict the step deformations. Obviously, all these local abnormalities have been well detected like normal fissures, as seen in the blending images and 3D visualization of fissure surfaces. A special case is shown by mark C, where a double line response occurs along the bright object because the thickened fissure was actually detected as two parallel step-edges. However, apart from lobar fissures, there also exist other redundant planar structures such as accessory fissures and borders of bullae (see the false positive detection around E). Because our intention is to preserve the large planar structures, these interference tissues cannot be expelled without further anatomy and global shape constraints.

III. DATA AND REFERENCES

We used two datasets for evaluation: Dataset 1 from our own department, which contains a complete 3D reference; and Dataset 2 with a limited reference, which is publicly available.

A. Dataset 1

The first dataset contains 23 chest CT scans of Chronic Obstructive Pulmonary Disease (COPD) patients (i.e., the GLU-COLD dataset) from a previous study [38]. The images were acquired with a Toshiba Aquilion 16 CT scanner using the parameters: 120 kVp; 140 mAs per rotation; rotation time 0.4 s; collimation: 16×0.5 mm; and pitch factor: 1.4375. Images were reconstructed with a FC02 kernel (FOV of 295–400 mm; slice thickness 0.5 mm; increment 0.5 mm). Scans were made during breath hold at full inspiration without contrast media. The patient group had moderate to severe COPD (GOLD stage II and III) without $\alpha 1$ antitrypsin deficiency; aged 49–78, and FEV1

between 36% and 87% predicted. The GLUCOLD scans are used with their left and right lungs being divided.

In previous work [39], we have utilized the GLUCOLD dataset to verify a lobe segmentation algorithm, where ground truth lobe segmentations were manually defined by one of the authors (M.E.B.). With inspection and approval from a pulmonologist (J.S.), the lobe references were gradually refined and finally established. Specifically, the lobe boundary reference was manually delineated slice by slice. If the fissure is invisible, they inferred the boundary from the distribution of pulmonary vessels and bronchi. Here, we adopt a morphological gradient operator to automatically extract the interlobar boundaries from the lobe references, which are directly used as ground truth for validation of fissure segmentation.

A lung mask is first defined by combining previous lobe references. Then, we adopt a model-based region growing algorithm [40] to extract the large airway and vessel lumen, and a further morphological dilation to cover its wall. Both lumen and wall are removed from the final lung mask, which will be used to confine the post-processing region as described in Section II-B.

B. Dataset 2

Dataset 2 was taken from the LObe and Lung Analysis 2011 (LOLA11) challenge [41], for which 55 volumetric chest CT scans were acquired from different sites, using several different scanners, scanning protocols, and reconstruction parameters. Most scans contain various pathologic abnormalities, ranging from mild to severe. The inplane resolution is between 0.53 mm and 0.78 mm whereas the slice thickness is between 0.3 mm and 1.5 mm.

The organizers of LOLA11 made a manual segmentation available of the lung lobes on 9 coronal slices for each case by two human observers. Both observers were instructed not to draw a lobar border when they felt it was not possible [15]. Until now, only two groups submitted their lobe segmentation results to the challenge website (http://www.lola11.com) without separate fissure segmentation [42], [15]. Because fissure detection is different from lobe segmentation, we need

specific and more accurate fissure references for evaluation, especially concerning the determination of visibility and location. Therefore, two co-authors (M.E.B. and J.S.) verified the LOLA11 reference, and removed parts of the fissures that were not visible on CT and added small visible parts that were missed in the LOLA11 reference. This was subsequently used as a ground truth in our experiments.

Here, the lung masks were constructed by firstly extracting the lung parenchyma with a global threshold binarization, then a morphological gap-closing operation was used to contain the small vessels and possible fissure regions. For normal scans, the above result is sufficient for non-lung interference elimination. But manual editing is indispensable for pathological cases like local high-intensity parenchyma and thickened fissures linking to the lung boundary. Our co-authors (M.E.B. and J.S.) conducted the final inspection and verification. Like the GLUCOLD dataset, we also removed the large bronchi and large pulmonary vessels from the lung masks using a region growing algorithm [40].

IV. EXPERIMENTS AND EVALUATION

In this section, the proposed DoS filter and segmentation algorithms are validated with the above-mentioned data sets and their references/ground truths. A hybrid coding with Mevislab [43], Matlab (MathWorks Inc.) and C + + was used for algorithms implementation and validation. The runtime of the DoS filter for a typical $256 \times 512 \times 512$ size 3D image is around 810s on our computer, configured with a 2.67 GHz CPU, 24 GB memory and a 64-bit Windows 7 operating system. For better reproducibility, the source code (Matlab version) of our filter will be open and publicly available on the Internet after the publication. We only considered the interlobar fissures (no accessory fissures), and the oblique and horizontal fissures in the right lung were treated as a single object.

As a comparison, a classical unsupervised filter of Wiemker *et al.* [19] and an updating line enhancing filter of Klinder *et al.* [27] were implemented for fissure enhancement with or without our proposed post-processing pipeline for final segmentation. The Wiemker filter is essentially a fissure likelihood function, which utilizes the Hessian or structure tensor to form a geometric representation of 3D planar shape and a Gaussian intensity windowing term is further merged to select the bright fissure objects. A single scale $\sigma = 1$ voxel is used for Hessian derivatives and eigenvalues calculation in our experiments following [21]. The Klinder line enhancing filter was presented as an improvement of the Wiemker filter using a multiple hypotheses testing template model. We implemented the Klinder filter using the same parameters as the original authors [27].

A. Evaluation Criteria

The quantitative evaluation was conducted mainly with Precision-Recall (PR) measures. Since we defined the references only for the lobar fissures, correctly detected accessory fissures would be counted as false positives. To minimize this influence, we defined a Volume of Interest (VoI) with a 40 mm width band around each reference, and the quantitative evaluation was confined only to the VoI region. Then, the voxels of the *binary result* inside the VoIs are classified as true positive (TP_1) or
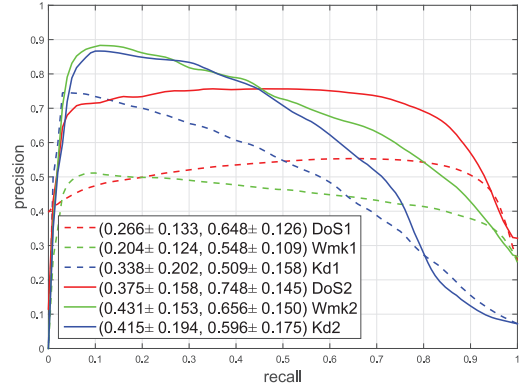

Fig. 7. Quantitative evaluation of fissure filtering using the mean Precision-Recall curves in the LOLA11 dataset (55 subjects). The proposed DoS filter is compared with the unsupervised filter of Wiemker (Wmk) [19] and the line enhancing filter of Klinder (Kd) [27]. DoS1/Wmk1/Kd1 and DoS2/Wmk2/Kd2 indicate the filters without and with a post-processing clutter removal, respectively. The average AUCs and max F_1-scores along with their standard deviations are given sequentially in the brackets of the legends.

false positive (FP) depending on their overlap with the reference. We used a 3 mm tolerance for determining the overlap, i.e., those with a distance less than 3 mm from the reference are considered TP_1 and the rest being FP. Accordingly, the *reference* pixels are divided into TP_2 and false negative (FN) using the same overlapping criterion, where FN corresponds to those located more than 3 mm from the binary result. Note the two true positive measures TP_1 and TP_2 are not always equal. To avoid the influence of unbalanced number of voxels, $Precision$ and $Recall$ are defined as $TP_1/(TP_1 + FP)$ and $TP_2/(TP_2 + FN)$, respectively. Subsequently, the F_1-score is derived from these values as $2Precision \cdot Recall/(Precision + Recall)$. Note the F_1-score is also known as the Sørensen-Dice coefficient, which indicates a similarity between the segmentation and reference. To distinguish the over- and under-segmentation errors, we particularly introduced a False Discovery Rate ($FDR = FP/(TP_1 + FP)$) and a False Negative Rate ($FNR = FN/(TP_2 + FN)$) as quantitative indices.

Note that the VoI based evaluation is a realistic scheme to circumvent the interference of unrelated planar tissues such as accessory fissures locating far away from the object. Although false positive responses outside the VoI region are simultaneously ignored, they actually have rare influence on typical applications like lobe segmentation.

B. Evaluation of Fissure Enhancement

The performance of the DoS fissure filtering was evaluated together with the Wiemker method [19] and Klinder filter [27] using the Precision-Recall curve. In the validations, we used a fixed parameter configuration $L = 11$, $S = 3$, $\kappa = 0.7$ for the DoS filtering. We first binarized the filtered images with different global thresholds gradually changing from minimum to maximum intensity, then the indices can be calculated without or with clutter removal, see Section IV-A for the criteria. The clutter removal was realized using the same branch-point detection and connected component analysis algorithms as our post-processing pipeline.

In Fig. 7, the PR curves from the LOLA11 data are presented, where the area under the PR curve (AUC) and the maximum
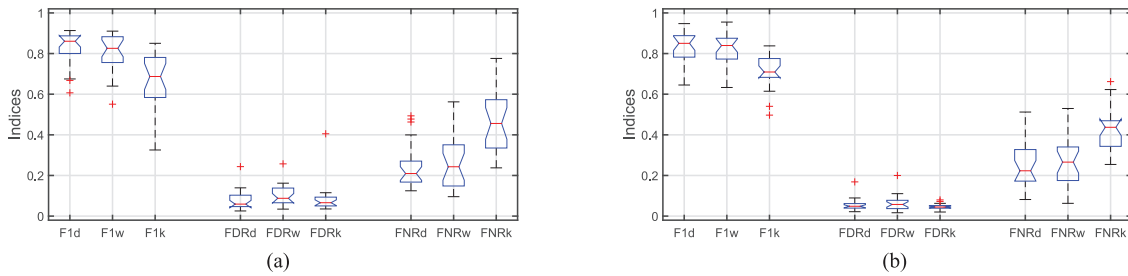
Fig. 8. Segmentation validation on the GLUCOLD dataset (23 subjects). Here, the boxplots are calculated with left and right lungs being separated. The F_1-score, FDR and FNR indices from the DoS (d), Wiemker (w) and Klinder (k) filtering segmentations are given sequentially in (a) and (b). The medians of boxplots are successively 0.885, 0.853, 0.687, 0.0738, 0.0711, 0.0659, 0.165, 0.234, 0.456 in (a); and 0.856, 0.841, 0.709, 0.0691, 0.0604, 0.0448, 0.204, 0.244, 0.437 in (b). (a) Left lung (b) Right lung.

F_1-score indices are given in the legends. Without clutters removal all the filters obtained very low indices, mainly ascribing to dense residual of interferences in the filtered images. The clutter removal largely improved the performance with the PR curves (DoS2, Wmk2 and Kd2) located entirely above their corresponding curves (DoS1, Wmk1 and Kd1) without post-processing. Generally the DoS filter outperformed the Wiemker and Klinder filters with higher max F_1-scores, although its AUC index is slightly lower after the clutter removal. Note the max F_1-score is the index directly linking to final optimal segmentation. Therefore, the tendency of PR curves at the top right corner is of more significant value in performance evaluation.

C. Validation of Fissure Segmentation

The segmentation performance was validated separately on the GLUCOLD and LOLA11 data sets. We first enhanced CT scans using the DoS, Wiemker or Klinder filter, then the multi-threshold postprocessing pipeline was applied to obtain final segmentations. A fixed set of thresholds 1, 5, 10, 20, 40 and 60 was used for post-processing of DoS filtered images, and the intensity of the Wiemker and Klinder filtered images was scaled to $[0, 80]$ before applying the same multiple threshold binarizations.

1) Dataset 1: Because the GLUCOLD data set contain fissure references for left and right lungs separately, the boxplots of F_1-score, FDR and FNR indices are separately calculated and illustrated. It can be found with the left lungs in Fig. 8(a) that the proposed DoS scheme obtained a higher median value and narrower interquartile range (IQR) of the F_1-scores than the Wiemker and Klinder schemes, and the difference between methods is more obvious in the FNR boxplots. For the right lungs in Fig. 8(b), the advantage of our proposed method appears comparable but the IQRs from the Wiemker and Klinder methods are slightly smaller compared to the left lung. In comparison, the higher FNR values indicate that more references were undetected in the Wiemker and Klinder methods.

We selected several examples of fissure segmentation respectively corresponding to high FDR, FNR and F_1 values for visual inspection, see Fig. 9. The extracted fissures are rendered in green, the references in yellow and their overlapped region in purple. In Figs. 9(a) and 9(d), the residual non-overlapped green patches, which are considered an over-segmentation, might

originate from accessory fissures or adhering clutters, resulting in a higher FDR. Because the interlobar boundary references contain invisible boundaries inferred from indirect information, the undetected large yellow regions in Figs. 9(b) and 9(e) might not definitely be visible fissures, but are all counted under-segmentations in our evaluation and thus raise the FNR indices to some extent. Two successful segmentations are shown in Figs. 9(c) and 9(f), where the predominantly purple areas indicate a high consistency between the segmentation and reference. As shown in the second row of Fig. 9, the main shortcoming of Wiemker filtering method is that the under-segmentations appear more serious than the DoS filter, which just verified its higher FNR indices in Fig. 8. Generally, the Klinder filter performed worse than the other two filters with more weak fissures being lost.

2) Dataset 2: Because the LOLA11 references were only defined on a few coronal slices for each scan, the computation of quantitative indices is also limited to these sparse slices. Using the same criteria in Section IV-A, we obtained the indices for the DoS, Wiemker and Klinder filters based segmentations (see Fig. 10). The boxplots reveal a decrease in performance with lower F_1-score, higher FDR and FNR for all the three filtering methods comparing to GLUCOLD data. But the decline of the Wiemker scheme is especially salient with a median F_1-score of 0.687 and a median FNR of 0.451. The Klinder filter performed the worst from the overall indices.

The deteriorated performance in the LOLA11 data comes from more complex factors like serious pathology, thick slice spacing, heavy imaging noise and different scanning protocols. Although the DoS filtering scheme also failed on a few extremely challenging cases (see the outliers of F1d in Fig. 10), its general performance is acceptable with a median F1-score of 0.833 and a median FDR of 0.102. The slightly increasing FNRs indicate that the fissures are more easily missed in the LOLA11 data.

For visual inspection, six scans corresponding to high F_1, FDR and FNR values among the DoS filtering segmentations are chosen for demonstration. We adopt the same rendering color map as in Fig. 9 (green: detected fissures, yellow: manual references, and purple: overlap regions). In Figs. 11(a) and 11(b), the dense planar clutters are considered the main sources of false responses and consequently raise the FDRs as an over-segmentation error. The obvious yellow stripes indicate a large missing area of interlobar references in Figs. 11(c) and
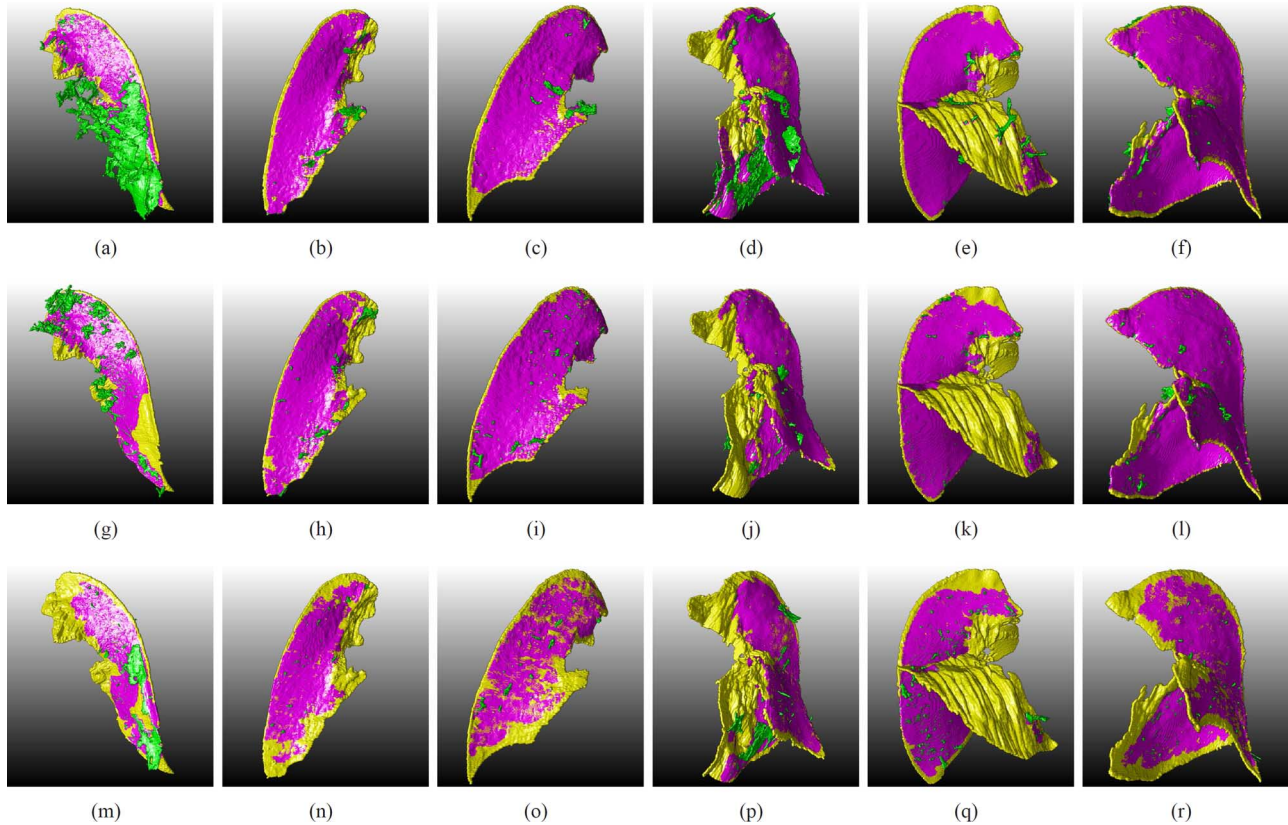
Fig. 9. Demonstration of fissure segmentation in the GLUCOLD data set. The upper row shows the results of the proposed method. Examples corresponding to high FDR (over-segmentation), FNR (under-segmentation) and F1-score indices are sequentially illustrated in (a)-(c) for the Left lungs and in (d)-(f) for the right lungs. For comparison, the second row gives the Wiemker filtering segmentations and the third row being the Klinder filtering segmentations. The segmented fissures are rendered in green color, the manual reference in yellow color and the purple color indicates the overlapping regions.
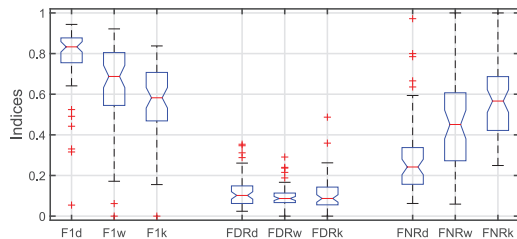

Fig. 10. Segmentation validation with the LOLA11 data set including 55 scans. The box-plots of indices corresponding to the DoS(d), Wiemker(w) and Klinder(k) filtering based segmentations are drawn next to each other in terms of F1-score, FDR and FNR, respectively. Here, the median values of boxplots are successively 0.833, 0.687, 0.582, 0.102, 0.087, 0.087, 0.242, 0.451 and 0.566.

11(d), and thus resulted in high FNRs. Two examples with high F_1-score values are given in Figs. 11(e) and 11(f), where the predominantly purple stripes indicate that the references are almost completely detected. As the references are slightly dilated for better visualization, the yellow and purple blending stripes are caused by small dislocation between the reference and segmentation. For comparison, the segmentations from the Wiemker filtering scheme are illustrated on the second row. Except the comparable results in Figs. 11(g) and 11(l), the Wiemker scheme resulted in very serious under-segmentations. The third row corresponds to the Klinder filter based segmentation, where a majority of results appear worse than the above filters except Fig. 11(n) is comparable to our segmentation.

D. Parameter Configuration

For the DoS filter, there are three parameters including the spacing width S, stick length L and interference suppression coefficient κ, that need be configured. Beforehand, we empirically fixed the spacing width to $S = 3$ according to the appearance of fissures in the clinical images.

The κ parameter should be chosen to suppress undesirable blob interferences while accommodating local fissure discontinuity. To verify its influence on fissure segmentation, we computed the F_1-score boxplots of LOLA11 segmentations from our proposed method using different κ and a fixed $L = 11$. It can be seen in Fig. 12(a) that the F_1-score median values are stable over a large range of $\kappa \in [0.2, 1.2]$ with the maximum locating at $\kappa = 0.7$. This means the proposed method is not sensitive to this parameter configuration, and $\kappa = 0.7$ is an optimal choice according to the experiments.

The stick length L is another important parameter. We calculated the F_1-score boxplots from the LOLA11 data experiments by varying the L parameter with a fixed $\kappa = 0.7$. As observed in Fig. 12(b), the difference among boxplots is small for $L \in [7, 17]$. The maximum of F_1-score medians appears at $L = 11$, which corresponds to the configuration used in our paper. Because the computation complexity of DoS filtering is $O(L^3)$, a larger L will saliently increase the computation time. Therefore, a small $L = 7$ might be a good choice for time critical applications.
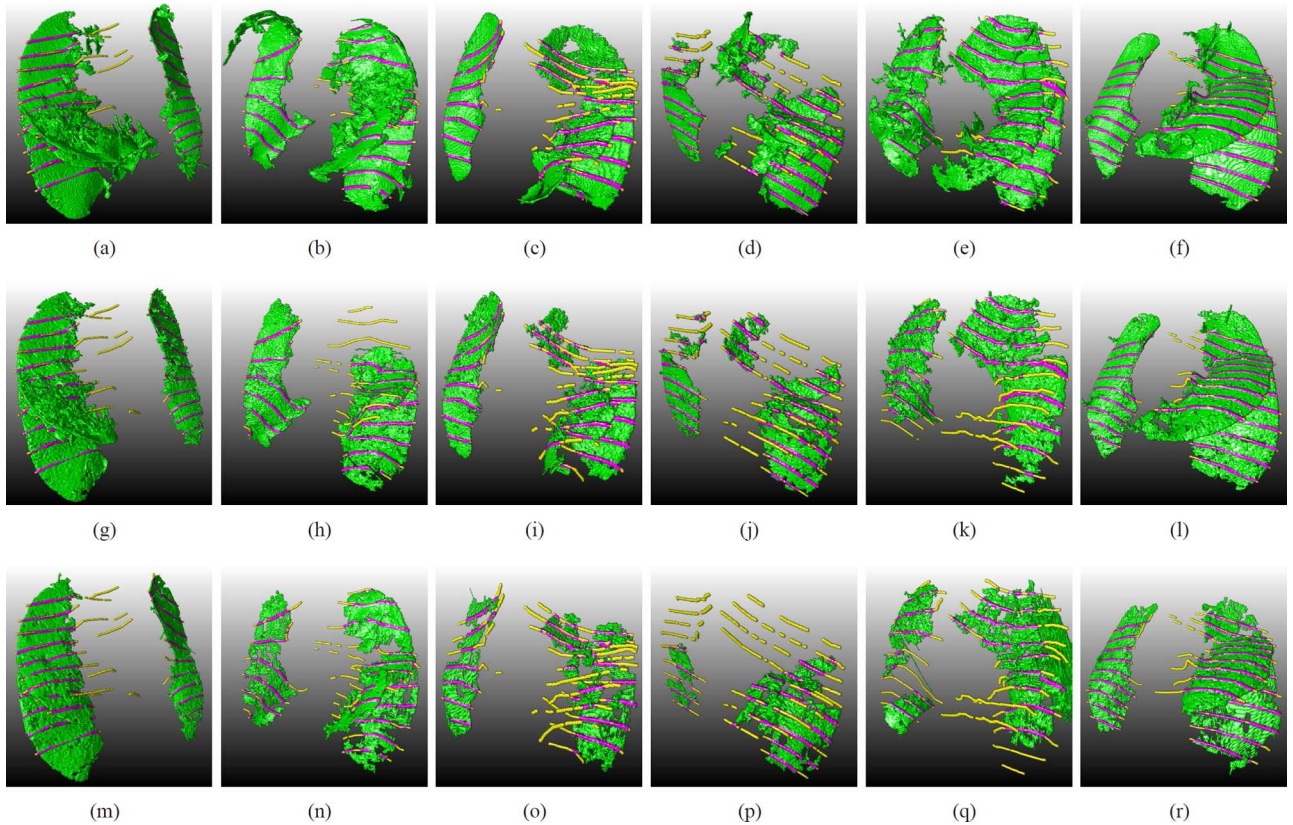
Fig. 11.   Demonstration of fissure segmentation in the LOLA11 data. The upper row shows the results of the proposed method. Examples of high FDR (a-b), FNR (c-d) and F1-score (e-f) indices are sequentially illustrated, corresponding respectively to case 27, 39, 26, 14, 22 and 41 from left to right. For comparison, the second row gives the Wiemker filtering segmentations and the third row being the Klinder filtering segmentations. Here, the segmentation results are rendered in green, the references in yellow and their overlapping regions in purple.
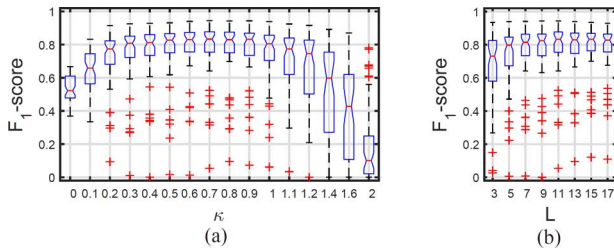

Fig. 12.   Box plots of our fissure segmentation with different parameters using the LOLA11 data. The medians of the boxplots are 0.830, 0.833, 0.830 for $\kappa = 0.6, 0.7, 0.8$ in (a), and 0.824, 0.833, 0.830 for $L = 9, 11, 13$ in (b). (a) Sensitivity of the κ parameter (b) Stick length L.

There are also several parameters in the post-processing pipeline. In this paper, a fixed set of binarizing thresholds b_i (1, 5, 10, 20, 40, 60) were chosen for both GLUCOLD and LOLA11 data. The volume threshold vT for branch-points removal is empirically selected to 100 voxels. For the final interlobar fissure segmentation, we introduced a volume sorting scheme to pick out the N biggest surface patches from the multi-threshold merging output. A parameter $N = 20$ is adopted for the LOLA11 data containing two lungs, and $N = 10$ for the single left or right lungs of GLUCOLD data.

V. DISCUSSION AND CONCLUSION

We proposed a derivative of stick filter and a post-processing segmentation pipeline for pulmonary fissures detection in tho-racic CT images. The principle of our filter originated from an observation that the 3D surface shape of fissures can be simplified to an equivalent co-linear constraint across multiple section planes. An obvious merit is that typical abnormalities including thickened fissure, step deformation and orientation deviations are well preserved with a distinct nonlinear derivatives combination and shape description. In the post-processing stage, the 3D continuity of the fissure surface is further exploited to separate adhering clutters by introducing a branch-point removal algorithm. Our additional contribution is to develop a multi-threshold merging framework to improve completeness of fissure detection.

The presented algorithms have been quantitatively evaluated on two large data sets containing 23 scans of COPD and 55 scans of different pathological human lungs. Both visual inspection and Precision-Recall curve analysis showed that the DoS filtering method gives superior results compared to two existing methods. In the fissure enhancement experiment, the DoS filter obtained an average max F_1-score that was 14% larger than the Wiemker filter and 25% larger than the Klinder filter. For the fissure segmentation validation, the median F_1-score values from the proposed method are 0.885, 0.856 and 0.833 for the single left lung and right lung from the GLUCOLD data, and both lungs from LOLA11 data, respectively. Generally, the good performance of our method is mainly ascribed to a lower FNR index, which means the completeness of fissure detection has been improved with the DoS filter. As far as we know, this is

the first validation of fissure detection using complete 3D references on such large data set.

An inherent limitation with our DoS filter comes from its interference suppression term formulated on intensity variance along the stick. Although this term can help to discriminate most objects from blob clutters, some seriously weak and noisy fissures, appearing as sparse and slightly bright point-cloud with a large intensity variance, are incorrectly suppressed and thus cause an undetection in subsequent segmentation. This phenomenon was mainly seen in the thick-slice (z-spacing ≥ 1.0 mm) and low-dose scans, e.g., LOLA11–06 and 07 data. Although these extremely weak fissures are still perceptually visible to our human observers, the computerized recognition of point-clouds like curvilinear structures remains an open issue [44]. In the post-processing stage, we adopted a simple volume sorting scheme for clutter removal. Because accessory fissures and planar clutters might have similar volumes as the lobar fissures, they are inevitable to be left over in the segmentation. This is considered an intrinsic drawback of direct fissure information based algorithms. In the validation, we adopted an interlobar boundary reference rather than the popular visible fissure reference used in previous work. The reason is that the judgement of visibility on weak fissures is actually quite inconsistent among different observers and might cause a large interobserver variability according to our testing. Correspondingly, our conservative definition of references will result in a biased increase of False Negative counts but provide a more objective standard for comparison, since the biases are equivalent to different algorithms.

As mentioned by previous authors [23], pulmonary fissure detection and lobe segmentation are two different tasks in spite of their close connection. Because the interlobar fissures often appear incomplete, we cannot expect to obtain a full lobe segmentation merely from the fissure detection. This fact is clearly illustrated in Fig. 9 with lobe fissures overlaying on their interlobar boundary reference. However, a direct application of our fissure detection algorithms could be quantitative estimation of fissure integrity [4], which corresponds to the ratio of visible fissures along the interlobar boundary.

In this paper, only the magnitude of DoS filter responses was utilized for line shape detection. But their directional field might provide more stable and continuous information along fissure profiles. It will be our future work to improve the performance by merging both magnitude and directional field responses. Additionally, our future work will introduce some prediction and verification mechanisms to improve the cloud-point objects detection on basis of the DoS filter. To achieve further lobe division, we will also pursue to automate lobar fissure selection by integrating pulmonary airway and artery tree locations.

REFERENCES

[1] A. Aziz, K. Ashizawa, K. Nagaoki, and K. Hayashi, "High resolution CT anatomy of the pulmonary fissures," *J. Thorac. Imag.*, vol. 19, no. 3, pp. 186–191, 2004.

[2] A. Yildiz *et al.*, "HRCT evaluation of the accessory fissures of the lung," *Eur. J. Radiol.*, vol. 49, no. 3, pp. 245–249, 2004.

[3] P. Cronin *et al.*, "Normal and accessory fissures of the lung: Evaluation with contiguous volumetric thin-section multidetector CT," *Eur. J. Radiol.*, vol. 75, no. 2, pp. E1–E8, 2010.

[4] J. Pu *et al.*, "Pulmonary fissure integrity and collateral ventilation in COPD patients," *PLoS ONE*, vol. 9, no. 5, p. E96631, 2014.

[5] E. van Rikxoort *et al.*, "A method for the automatic quantification of the completeness of pulmonary fissures: Evaluation in a database of subjects with severe emphysema," *Eur. Radiol.*, vol. 22, no. 2, pp. 302–309, 2012.

[6] I. Sluimer, A. Schilham, M. Prokop, and B. Van Ginneken, "Computer analysis of computed tomography scans of the lung: A survey," *IEEE Trans. Med. Imag.*, vol. 25, no. 4, pp. 385–405, Apr. 2006.

[7] J.-M. Kuhnigk, "Lung lobe segmentation by anatomy-guided 3d watershed transform," in *Proc. SPIE Med. Imag.*, 2003, pp. 1482–1490.

[8] S. Ukil and J. M. Reinhardt, "Anatomy-guided lung lobe segmentation in x-ray CT images," *IEEE Trans Med. Imag.*, vol. 28, no. 2, pp. 202–214, Feb. 2009.

[9] X. Zhou *et al.*, "Automatic segmentation and recognition of anatomical lung structures from high-resolution chest CT images," *Comput. Med. Imag. Graph.*, vol. 30, no. 5, pp. 299–313, 2006.

[10] Q. Wei, Y. Hu, G. Gelfand, and J. H. Macgregor, "Segmentation of lung lobes in high-resolution isotropic CT images," *IEEE Trans. Biomed. Eng.*, vol. 56, no. 5, pp. 1383–1393, May 2009.

[11] V. Appia, U. Patil, and B. Das, "Lung fissure detection in CT images using global minimal paths," in *Proc. SPIE Med. Imag.*, 2010, pp. 76231P–76231P.

[12] Q. Wei, Y. Hu, J. H. MacGregor, and G. Gelfand, "Automatic recognition of major fissures in human lungs," *Int. J. Comput. Assist. Radiol. Surg.*, vol. 7, no. 1, pp. 111–123, 2012.

[13] L. Zhang *et al.*, "Atlas-driven lung lobe segmentation in volumetric x-ray CT images," *IEEE Trans. Med. Imag.*, vol. 25, no. 1, pp. 1–16, Jan. 2006.

[14] E. M. Van Rikxoort *et al.*, "Automatic segmentation of pulmonary lobes robust against incomplete fissures," *IEEE Trans. Med. Imag.*, vol. 29, no. 6, pp. 1286–1296, Jun. 2010.

[15] B. Lassen *et al.*, "Automatic segmentation of the pulmonary lobes from chest CT scans based on fissures, vessels, and bronchi," *IEEE Trans. Med. Imag.*, vol. 32, no. 2, pp. 210–222, Feb. 2013.

[16] S. Gu *et al.*, "Identification of pulmonary fissures using a piecewise plane fitting algorithm," *Comput. Med. Imag. Graph.*, vol. 36, no. 7, pp. 560–571, 2012.

[17] M. Kubo *et al.*, "Extraction algorithm of pulmonary fissures from thin-section CT images based on linear feature detector method," *IEEE Trans. Nucl. Sci.*, vol. 46, no. 6, pp. 2128–2133, Dec. 1999.

[18] S. Saita *et al.*, "An algorithm for the extraction of pulmonary fissures from low-dose multislice CT image," *Syst. Comput. Jpn.*, vol. 37, no. 9, pp. 63–76, 2006.

[19] R. Wiemker, T. Bülow, and T. Blaffert, "Unsupervised extraction of the pulmonary interlobar fissures from high resolution thoracic CT data," in *Int. Congr. Series.* New York: Elsevier, 2005, vol. 1281, pp. 1121–1126.

[20] Q. Li, S. Sone, and K. Doi, "Selective enhancement filters for nodules, vessels, and airway walls in two-and three-dimensional CT scans," *Med. Phys.*, vol. 30, no. 8, pp. 2040–2051, 2003.

[21] E. M. Van Rikxoort, B. Van Ginneken, M. Klik, and M. Prokop, "Supervised enhancement filters: Application to fissure detection in chest CT scans," *IEEE Trans. Med. Imag.*, vol. 27, no. 1, pp. 1–10, Jan. 2008.

[22] E. M. Van Rikxoort, B. De Hoop, S. Van De Vorst, M. Prokop, and B. Van Ginneken, "Automatic segmentation of pulmonary segments from volumetric chest CT scans," *IEEE Trans. Med. Imag.*, vol. 28, no. 4, pp. 621–630, Apr. 2009.

[23] J. Pu *et al.*, "A computational geometry approach to automated pulmonary fissure segmentation in CT examinations," *IEEE Trans. Med. Imag.*, vol. 28, no. 5, pp. 710–719, May 2009.

[24] J. Pu *et al.*, "Computerized assessment of pulmonary fissure integrity using high resolution CT," *Med. Phys.*, vol. 37, no. 9, pp. 4661–4672, 2010.

[25] J. C. Ross, "Automatic lung lobe segmentation using particles, thin plate splines, and maximum a posteriori estimation," in *Proc. MICCAI*, 2010, pp. 163–171.

[26] J. C. Ross *et al.*, "Pulmonary lobe segmentation based on ridge surface sampling and shape model fitting," *Med. Phys.*, vol. 40, no. 12, p. 121903, 2013.

[27] T. Klinder, H. Wendland, and R. Wiemker, "Lobar fissure detection using line enhancing filters," in *Proc. SPIE Med. Imag.*, 2013, p. 86693C.

[28] R. N. Czerwinski, D. L. Jones, and W. D. O'brien, "Line and boundary detection in speckle images," *IEEE Trans. Image Process.*, vol. 7, no. 12, pp. 1700–1714, Dec. 1998.

[29] C. Xiao, M. Staring, J. Wang, D. P. Shamonin, and B. C. Stoel, "A derivative of stick filter for pulmonary fissure detection in CT images," in *Proc. SPIE Med. Imag.*, 2013, p. 86690V.

[30] Y.-K. Lee and W. T. Rhodes, "Rotating-kernel min-max algorithms for straight-line feature enhancement," *Appl. Opt.*, vol. 34, no. 2, pp. 290–298, 1995.

[31] C.-Y. Xiao, Z. Su, and Y.-Z. Chen, "A diffusion stick method for speckle suppression in ultrasonic images," *Pattern Recognit. Lett.*, vol. 25, no. 16, pp. 1867–1877, 2004.

[32] C. Xiao *et al.*, "A strain energy filter for 3d vessel enhancement with application to pulmonary CT images," *Med. Image Anal.*, vol. 15, no. 1, pp. 112–124, 2011.

[33] A. F. Frangi, W. J. Niessen, K. L. Vincken, and M. A. Viergever, "Multiscale vessel enhancement filtering," in *MICCAI'98*, 1998, pp. 130–137.

[34] A. Hunter *et al.*, "Tram-line filtering for retinal vessel segmentation," in *IFMBE Proc. 3rd Eur. Med. Biol. Eng. Conf.*, 2005, vol. 11.

[35] C. Xiao, M. Staring, Y. Wang, D. P. Shamonin, and B. C. Stoel, "Multiscale bi-Gaussian filter for adjacent curvilinear structures detection with application to vasculature images," *IEEE Trans. Image Process.*, vol. 22, no. 1, pp. 174–188, Jan. 2013.

[36] L. Lam, S.-W. Lee, and C. Y. Suen, "Thinning methodologies-a comprehensive survey," *IEEE Trans. Pattern Anal. Mach. Intell.*, vol. 14, no. 9, pp. 869–885, Sep. 1992.

[37] G. Papari and N. Petkov, "Adaptive pseudo dilation for gestalt edge grouping and contour detection," *IEEE Trans. Image Process.*, vol. 17, no. 10, pp. 1950–1962, Oct. 2008.

[38] T. S. Lapperre *et al.*, "Relation between duration of smoking cessation and bronchial inflammation in COPD," *Thorax*, vol. 61, no. 2, pp. 115–121, 2006.

[39] D. Shamonin *et al.*, "Automatic lung lobe segmentation of COPD patients using iterative b-spline fitting," in *Proc. SPIE Med. Imag.*, 2012, p. 83140W.

[40] E. Smistad, A. C. Elster, and F. Lindseth, "GPU accelerated segmentation and centerline extraction of tubular structures from MEDICAL images," *Int. J. Comput. Assist. Radiol. Surg.*, vol. 9, no. 4, pp. 561–575, 2014.

[41] E. Van Rikxoort and B. Van Ginneken, "Automatic segmentation of the lungs and lobes from thoracic CT scans," in *Proc. 4th Int. Workshop Pulmonary Image Anal*, 2011, pp. 261–268.

[42] B. Lassen, J.-M. Kuhnigk, M. Schmidt, S. Krass, and H.-O. Peitgen, "Lung and lung lobe segmentation methods at Fraunhofer mevis," presented at the 4th Int. MICCAI Workshop Pulmonary Image Anal., Toronto, Canada, 2011.

[43] F. Ritter *et al.*, "Medical image analysis: A visual approach," *IEEE Pulse*, vol. 2, no. 6, pp. 60–70, 2011.

[44] C. Becker, R. Rigamonti, V. Lepetit, and P. Fua, "Supervised feature learning for curvilinear structure segmentation," in *Proc. MICCAI*, 2013, pp. 526–533.